LANGMUIR Article
Cite This: Langmuir XXXX, XXX, XXX−XXX
pubs.acs.org/Langmuir

Kinetics of Nanoparticle−Membrane Adhesion Mediated by Multivalent Interactions

Roberta Lanfranco,*[,†,‡] Pritam Kumar Jana,[§] Lucia Tunesi,[†] Pietro Cicuta,[†] Bortolo Matteo Mognetti,[§] Lorenzo Di Michele,*[,†] and Gilles Bruylants*[,‡]

[†]Biological and Soft Systems, Cavendish Laboratory, University of Cambridge, JJ Thomson Avenue, Cambridge CB3 0HE, United Kingdom

[‡]Université Libre de Bruxelles (ULB), Engineering of Molecular NanoSystems, 50 av. F.D. Roosevelt, 1050 Brussels, Belgium

[§]Université Libre de Bruxelles (ULB), Interdisciplinary Center for Nonlinear Phenomena and Complex Systems, Campus Plaine, CP 231, Blvd. du Triomphe, B-1050 Brussels, Belgium

Supporting Information

ABSTRACT: Multivalent adhesive interactions mediated by a large number of ligands and receptors underpin many biological processes, including cell adhesion and the uptake of particles, viruses, parasites, and nanomedical vectors. In materials science, multivalent interactions between colloidal particles have enabled unprecedented control over the phase behavior of self-assembled materials. Theoretical and experimental studies have pinpointed the relationship between equilibrium states and microscopic system parameters such as the ligand−receptor binding strength and their density. In regimes of strong interactions, however, kinetic factors are expected to slow down equilibration and lead to the emergence of long-lived out-of-equilibrium states that may significantly influence the outcome of self-assembly experiments and the adhesion of particles to biological membranes. Here we experimentally investigate the kinetics of adhesion of nanoparticles to biomimetic lipid membranes. Multivalent interactions are reproduced by strongly interacting DNA constructs, playing the role of both ligands and receptors. The rate of nanoparticle adhesion is investigated as a function of the surface density of membrane-anchored receptors and the bulk concentration of nanoparticles and is observed to decrease substantially in regimes where the number of available receptors is limited compared to the overall number of ligands. We attribute such peculiar behavior to the rapid sequestration of available receptors after initial nanoparticle adsorption. The experimental trends and the proposed interpretation are supported by numerical simulations.

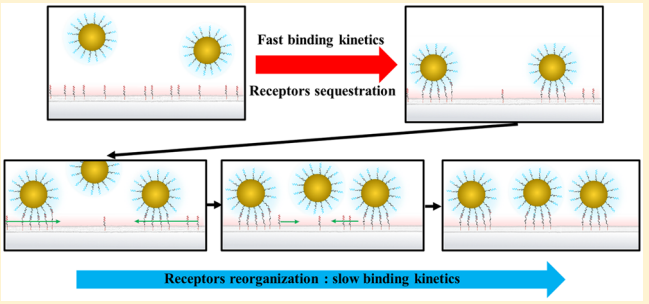

INTRODUCTION

Adhesive interactions between nanoscale objects and lipid membranes are central to a number of biological processes, including cell−cell communication mediated by extracellular vesicles,[1−3] viral infection,[4−6] and endocytosis.[7−9] In therapeutic and diagnostic nanomedicine, finding reliable strategies to control the interaction between biological membranes and nanoscale probes is a key issue.[10−12] Adhesion is often mediated by specific ligands on the surface of the nano-objects that target specialized receptors expressed on the cell membranes. The resulting multivalent interactions, mediated by a large number of interacting molecular agents, give rise to complex phase behaviors, which emerge from the interplay between enthalpic contributions to individual ligand/receptor interactions and configurational/combinatorial entropic effects.[13−18] The (bio)physics of multivalent interactions has been thoroughly characterized both experimentally and theoretically by means of analytical and numerical approaches.[15,18−22] In the context of materials science, the acquired understanding enabled the design of colloidal or nanoscale units, whose self-assembly behavior can be precisely prescribed.[23−28] In targeted drug delivery, multivalent interactions can be exploited to improve the binding selectivity of vectors, which can be designed to target cell membranes only if certain receptors are overexpressed, allowing one to discern between healthy and diseased cells.[29−32]

Our current understanding of the equilibrium features of multivalent systems[33] is not matched by systematic studies of kinetic effects, which are often relevant in regimes where ligand-mediated interactions become sufficiently strong, driving the system into long-lived metastable configurations that differ substantially from the equilibrium ground state. Interactions of such strength can occur in biological recognition schemes, where ligand−receptor binding free energies can exceed 25 k_BT.[34] In multivalent colloidal systems, kinetic arrest has been characterized and exploited to design

Received: August 9, 2018
Revised: January 4, 2019
Published: January 14, 2019

DOI: 10.1021/acs.langmuir.8b02707
Langmuir XXXX, XXX, XXX−XXX

self-protected interaction schemes or sequential self-assembly protocols.[35−39] However, with the exception of a limited number of studies[40−45] including the recent investigation of the adhesion kinetics of DNA-functionalized poly(amidoamine) dendrimers to solid surfaces,[46,47] systematic quantitative investigations have not been reported for the kinetics of multivalent nanoparticle−surface interactions. Particularly significant and unexplored is the role of kinetic effects in the presence of mobile linkers, and studies in this direction will be relevant to the understanding and design of the aforementioned biological and nanomedical processes.

In this article, we present a quantitative investigation of the adsorption kinetics of nanoparticles to biomimetic lipid membranes. In the adopted model system, large unilamellar lipid vesicles (LUVs) are targeted by gold nanoparticles (NPs), and complementary DNA constructs anchored on both substrates play the role of ligands and receptors, where the latter are able to freely diffuse, as in many biologically relevant situations.[15,48−53] The programmability and selectivity of Watson−Crick base pairing ensure accurate control of bond formation, enabling a quantitative characterization of kinetic effects as a function of different parameters characterizing the ligands, the receptors, and their complexes. Using dynamic light scattering (DLS), the nanoparticle adsorption kinetics is characterized as a function of the surface density of membrane-anchored DNA receptors as well as the overall bulk concentration of nanoparticles. We observe a substantial reduction of the adsorption rates in regimes where the number of available receptors is limited compared to the number of nanoparticles. The observed trend is ascribed to the rapid and nearly irreversible sequestration of most of the initially available receptors following the adsorption of a relatively small number of nanoparticles. Receptor depletion is a direct consequence of the mobility of membrane-anchored DNA linkers and is also expected to occur in biological systems where adhesion is mediated by proteins that can diffuse in the membrane. Experimental evidence is backed up by state-of-the-art simulations that accurately account for the effect of molecular reaction rates on the adsorption dynamics of the nanoparticles.

Our findings demonstrate that, in the presence of strong ligand−receptor interactions, factors such as receptor mobility and concentration should be taken into account when designing nanoscale probes for membrane targeting.

MATERIALS AND EXPERIMENTAL METHODS

DNA Ligands and Receptors. Single-stranded DNA was purchased from IDT (Integrated DNA Technologies, Leuven, Belgium). Strands mimicking ligands (5′-TGC GTG TGT GCG TTT TTT TTT T-3′-thiol) feature a thiol modification on their 3′ end, enabling grafting to gold NPs. Receptor strands (56FAM-5′TCG CAC ACA CGC TTTT TTT TTT-3′-chol) are modified with both a fluorescein (56FAM, 5′) and a cholesterol molecule (chol, 3′) (Figure 1). The latter is connected to the DNA via a triethylene glycol (TEG) spacer and enables grafting onto lipid bilayers. Ligand and receptor strands feature mutually complementary sticky ends of 11 nucleotides, driving their hybridization and NP-membrane adhesion. Poly-T domains are included between the sticky overhangs and the grafting moieties to improve configurational freedom.

Liposome Preparation, Functionalization, and Characterization. Large unilamellar vesicles (LUVs) were prepared from 1-palmitoyl-2-oleoyl-glycero-3-phosphocholine (POPC) lipids (Avanti Polar Lipids, CAS number 26853-31-6) by membrane extrusion using an Avanti miniextruder. First, a dry lipid film is obtained by the evaporation of a chloroform solution under vacuum for 1 h. The lipid

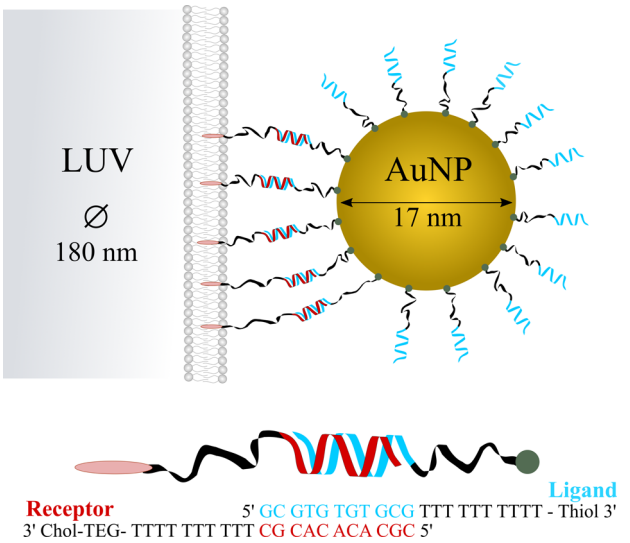

Figure 1. Hybridization between DNA ligands and receptors drives the adhesion of a NP to a lipid membrane. The sequences of ligand and receptor DNA strands are reported. They feature, respectively, a thiol and a TEG-cholesterol moiety to anchor them to NPs and LUVs.

film is then rehydrated with experimental buffer (10 mM phosphate buffer pH 7.4 + 0.5 M NaCl). Rehydration is facilitated by vortex mixing the sample for 1 min and further incubating for 1 h. The solution is then extruded 31 times through a polycarbonate membrane featuring track-etched pores with a diameter of 200 nm (Whatman). A large number of extrusion steps is necessary to obtain a homogeneous size distribution of the liposomes. As prescribed by the manufacturer of the extrusion kit (Avanti Polar Lipids), an odd number of steps are required so that any particulate contaminant larger than the pore size is blocked by the membrane and removed from the sample. The formed liposomes have a hydrodynamic diameter, measured with DLS (Malvern Zetasizer NanoZS, Malvern, U.K.), of either 160 ± 31 or 189 ± 37 nm (SI, section 1.1). The overall lipid concentration (2 mM) and the hydrodynamic diameter were used to estimate the bulk concentration of the liposomes. Vesicles were functionalized with different concentrations of receptor strands to obtain surface densities in a biologically relevant range[54,55] (SI, section 1.2). Functionalization was performed by adding DNA receptors to the LUV solution and agitating on an Eppendorf thermomixer for 16 h at 750 rpm. The cholesterol moiety spontaneously inserts into the lipid bilayer, providing a mobile but stable anchoring.[56−58] To demonstrate the grafting of all DNA strands to the LUVs, samples were analyzed by ultracentrifugation (Optima LE-80K from Beckman) in a sucrose gradient (SI, section 1.3).

NPs Synthesis, Functionalization, and Characterization. The materials used to synthesize NPs were potassium gold(III) tetrachloride ($KAuCl_4$, CAS no. 450235), dithiothreitol (DTT, CAS no. 3483-12-3), trisodium citrate ($Na_3C_6H_5O_7$, CAS no. 51 804), and Tris-HCl buffer (1 M, pH 7, CAS no. T6455) and were purchased from Sigma-Aldrich, while phosphate buffer and NaCl used for particle functionalization were purchased from Merck. Gold nanoparticles (NPs) were produced via a modified Turkevich method[59] and immediately dialyzed against a 0.1 mM citrate solution. The nanoparticles were characterized by TEM, UV−vis absorption, and DLS measurements, as reported in SI, section 2. An average diameter of 16.5 ± 1.3 nm was determined by analyzing TEM images with ImageJ. NPs were then functionalized with DNA ligands using thiol chemistry.[60] The grafting density was estimated by measuring the DNA concentration of the supernatant after a 20 min centrifugation step at 18 000 *g*. The concentration of DNA in the supernatants after the first washing step was measured to be 2.24 μM, while the initial DNA concentration was 3.23 μM, demonstrating the occurrence of DNA grafting. Afterward, the same washing procedure was repeated

DOI: 10.1021/acs.langmuir.8b02707
Langmuir XXXX, XXX, XXX−XXX

five times to remove all the nongrafted DNA. We obtained an average of 300 ligand strands per NP. The presence of a DNA layer on NPs was confirmed by both DLS and UV−vis, as reported in SI, section 2.

Characterizing the NP−LUV Adhesion and the Dissociation Temperature. The adhesion of NPs to LUVs was confirmed by means of UV−vis absorption spectroscopy (Schimadzu UV-3600 equipped with a Peltier temperature controller) monitoring the shift in the wavelength of the NP extinction peak induced by the reciprocal proximity between LUV-bound NPs. The dissociation temperature of the NP−LUV complexes was also determined and found to increase with increasing surface density of the receptors ρ_{R-LUV}. Details are provided in the SI, section 3.

Characterizing NP−LUV Adhesion with Dynamic Light Scattering. Experiments to monitor the adhesion kinetics of NPs to LUVs were carried out using dynamic light scattering (DLS). Initially, a sample of DNA-functionalized NPs in 0.5 M NaCl + 10 mM phosphate buffer at concentrations reported in the List of Samples section, typically in the range of 0.1−0.2 nM, was characterized via DLS. The scattering autocorrelation function (ACF) was used to quantify the diffusion parameters of free NPs, discussed in the Results and Discussion section. Then, LUVs were added to reach the target NP:LUV bulk concentration ratio $R_{NP:LUV}$, and the sample was rapidly mixed with a pipet. DLS data acquisition typically started 10 s after mixing, and 60 ACFs were acquired at 5 s intervals. The time interval between subsequent measurements was then increased to 30 s, 3 min, and 15 min to monitor adhesion over the following 14 h. All measurements were performed at 25 °C and 0.5 M NaCl ionic strength. A higher-than-physiological ionic strength was used in this study to obtain sufficiently high ligand−receptor binding strength to allow the emergence of significant kinetic effects associated with the near-irreversibility of the NP adhesion to the target vesicles.[61] The effect of a higher-than-physiological ionic strength is largely limited to the DNA-hybridization free energy, and therefore our results are readily applicable to any system with comparably strong ligand−receptor interactions, regardless of the ionic strength. Similar ionic conditions are routinely used in DNA nanosystems to make DNA duplexes more stable.[62−65]

List of Samples. A number of samples were tested with different surface concentrations of receptors on the LUVs, ρ_{R-LUV}, spanning a biologically relevant range,[54,55] and different NP:LUV bulk concentration ratios, $R_{NP:LUV}$. All tested conditions are listed in Table 1. For samples with $R_{NP:LUV}$ = 7 and 70, the bulk nanoparticles concentration ρ_{NP} is 1.1 × 10^{-10} M, while $R_{NP:LUV}$ = 290 corresponds to ρ_{NP} = 2.2 × 10^{-10} M.

Table 1. List of Tested Samples[a]

sample	$R_{NP:LUV}$	ρ_{R-LUV} (nm^{-2})	N_{R-LUV}	N_{R-NP}
1	7	3.9 × 10^{-3}	370	53
2	7	8.2 × 10^{-3}	770	110
3	7	12.7 × 10^{-3}	1190	170
4	7	17.5 × 10^{-3}	1640	234
5	70	3.9 × 10^{-3}	370	5
6	70	8.2 × 10^{-3}	770	11
7	70	12.7 × 10^{-3}	1190	17
8	70	17.5 × 10^{-3}	1640	23
9	290	3.9 × 10^{-3}	370	1
10	290	8.2 × 10^{-3}	770	3
11	290	12.7 × 10^{-3}	1190	4
12	290	17.5 × 10^{-3}	1640	6

[a] $R_{NP:LUV}$ indicates the NP:LUV bulk concentration ratio; ρ_{R-LUV}, the average surface concentration of receptors on the LUVs; N_{R-LUV}, the average total number of receptors on each LUV; and N_{R-NP} = $N_{R-LUV}/R_{NP:LUV}$, the average number of receptors available for each NP in the system. The number of ligands on each nanoparticle is fixed and equal to 300. See the SI, section 1.2, for details on the estimation of these values.

SIMULATION ALGORITHM

We model NPs as hard spheres freely diffusing in a parallelepipedal simulation box (Figure 2). Nanoparticles

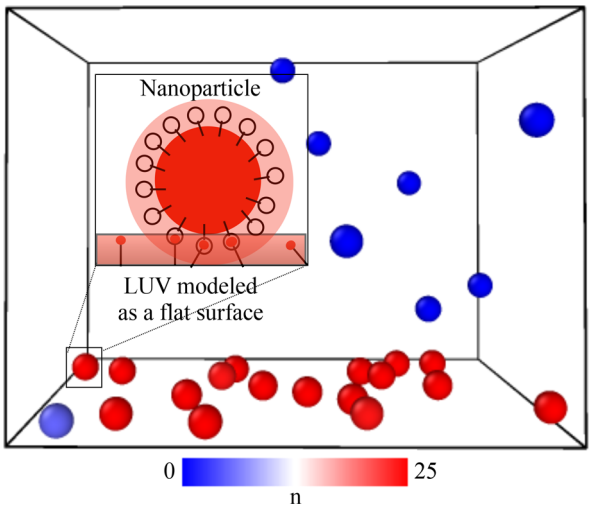

Figure 2. Modeling ligand−receptor-mediated interactions between NPs and membranes. Ligand and receptor sticky ends are uniformly distributed in the red-stained regions surrounding the NP and the membrane surface. (Inset) Simulation snapshot showing NPs anchored at the surface or freely diffusing in the bulk. The color map represents the number of formed NP−membrane bonds.

interact with the basal surface of the simulation box having an area A equal to that of a LUV. The surface carries N_{R-LUV} receptors, a number compatible with the one used in experiments. As often done when modeling DNA-functionalized surfaces,[16,18] we neglect receptor−receptor, receptor−ligand, and ligand−ligand steric interactions. We assume that the sticky ends tethered to the surface of the LUV are uniformly distributed and capable of free diffusion within a layer of thickness l = 3 nm surrounding the surface of the LUV (Figure 2). l has been estimated using typical end-to-end distances of ssDNA.[66] Similarly, nucleic acids on the NPs are simulated as N_{L-NP} sticky ends uniformly distributed within a shell of thickness l surrounding the particle (Figure 2). Given that in our modeling all ligands can bind, N_{L-NP} has been estimated by calculating the maximum number of ligands that could bind the surface using a geometrical construction (SI, section 4). To improve the computational efficiency, the ligands are also regarded as freely diffusive rather than anchored to a point on the NP surface. This approximation has a negligible effect on the results of this work. We apply the simulation algorithm presented in ref 67 to study the DNA-directed self-assembly of LUVs, adapted to the present system. Improving on conventional algorithms, our method synchronizes the binding kinetics of DNA with the diffusion kinetics of the nanoparticles, enabling one to study the effects of finite interaction rates on the adsorption kinetics. Note that our model does not account for the deformability of the LUVs. While membrane deformability is certainly pivotal in processes such as endocytosis[68−73] and membrane-mediated interaction between bound particles,[74,75] it is expected to play a small role in the present study to the extent that reactions between different ligand−receptor pairs can be considered to be independent events. We have verified this hypothesis in a recent publication[19] using a more detailed model accounting

DOI: 10.1021/acs.langmuir.8b02707
Langmuir XXXX, XXX, XXX−XXX

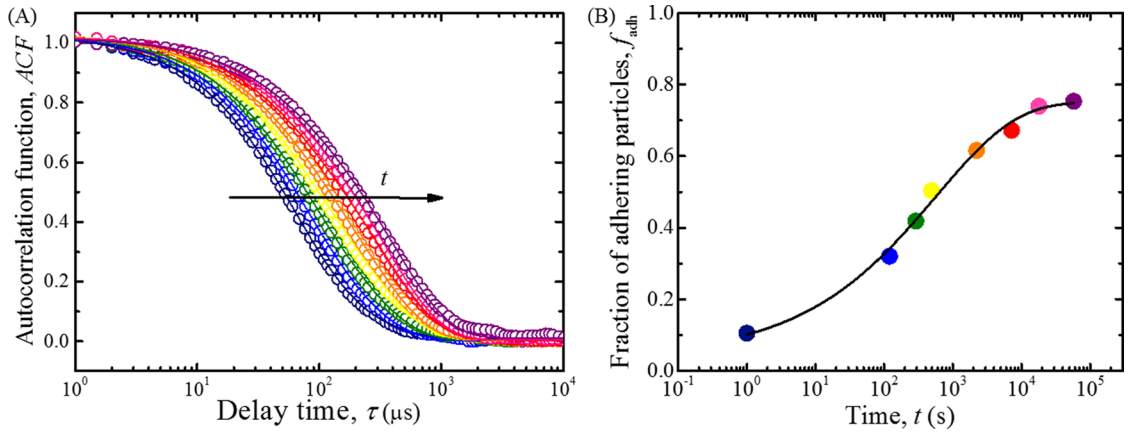

Figure 3. Quantifying adhesion kinetics with DLS. (A) Autocorrelation functions acquired with DLS for a system with $R_{NP:LUV} = 70$ and $\rho_{R-LUV} = 17.5 \times 10^{-3}$ nm^{-2}. The ACF was collected after different times t at the mixing LUVs and NPs (dark blue $t = 0$ s, light blue $t = 120$ s, green $t = 290$ s, yellow $t = 490$ s, orange $t = 2220$ s, red $t = 7200$ s, pink $t = 18\,000$ s, and purple $t = 57\,600$ s). (B) Fraction of bound NPs, f_{adh}, obtained by fitting the data from panel A with eq 6, extracting the two amplitudes $A_{free}(t)$ and $A_{adh}(t)$, and using eq 7. The color code is the same as in panel A. The fractions of adhering nanoparticles, f_{adh}, for all of the perfomed experiments are reported in the SI, section 9, Figure S9.1. Notice that only a subset of the collected ACFs are reported in panel A.

for membrane deformability. We also notice that an eventual wrapping of the NPs by the lipid bilayer would not change the conclusions of this article. Indeed, here we assume how receptors, once bound, no longer participate in the later stages of the adsorption. This scenario is not affected by the NPs being wrapped or not.

Nanoparticle positions ($\mathbf{r}_i$) are updated ($\mathbf{r}_i \rightarrow \mathbf{r}_i + \Delta\mathbf{r}_i$) using a Brownian dynamics scheme

$$\Delta\mathbf{r}_i = \mathbf{r}_i(t + \Delta t) - \mathbf{r}_i(t) = \mathbf{f}_i\frac{D}{k_B T}\Delta t + \sqrt{D\Delta t}\,\mathcal{N}(0, 1) \tag{1}$$

where $\mathbf{f}_i$ is the total force acting on NP i, D is the nanoparticle bulk diffusion coefficient under dilute conditions (estimated using the Stokes−Einstein equation as 2.8×10^7 nm^2 s^{-1}), Δt is the integration step, $\mathcal{N}$ is a vector of independent normally distributed numbers, k_B is the Boltzmann constant, and the index i labels individual NPs. In the (very dilute) bulk (Figure 2), nanoparticles repel each other through a short-range force $\mathbf{f}_{ij}$ due to the entropic compression of grafted DNA.[18] $\mathbf{f}_i$ (eq 1) is then given by $\mathbf{f} = \mathbf{f}_{R,i} + \sum_j \mathbf{f}_{ij}$, where $\mathbf{f}_{R,i}$ is the force between the surface and NP i

$$\mathbf{f}_{R,i} = k_B T[n_i^s\Gamma_1(\{\mathbf{r}\}) - n^s\Gamma_2(\{\mathbf{r}\}) - n_i\Gamma_3(\{\mathbf{r}\})] \tag{2}$$

In eq 2, n_i^s is the number of ligand−receptor bonds between nanoparticle i and the membrane, n^s is the number of free receptors, and n_i is the number of free ligands on particle I. Γ_1, Γ_2, and Γ_3 are geometric factors and have been derived in the SI, section 4.

We estimate n_i^s, n^s, and n_i using the Gillespie method.[76] At a given configuration $\{\mathbf{r}\}$, we calculate all of the on/off rates (k_{on}^i/k_{off}^i) of forming/breaking a bond between nanoparticle i and the membrane, with the assumption that $k_{on}^i = k_{off}^i = 0$ if nanoparticle i is not in contact with the interface. In the SI, section 4, we prove that[39]

$$k_{on}^i = k_{on}^0\lambda_i(\{\mathbf{r}\}),\ k_{off}^i = k_{on}^0\rho_0\exp[\beta\Delta G_0] \tag{3}$$

where $\lambda_i(\{\mathbf{r}\})$ represents geometrical factors (SI, section 4), ΔG_0 is the hybridization free energy of free sticky ends in solution,[61] $\beta = 1/k_B T$, k_{on}^0 is the on rate of the sticky ends, and ρ_0 is the standard concentration, which is equal to 1 mole per liter. In the following text, we report the on rates in simulation units: $k_{on}^{0,*} = k_{on}^0\rho_0 l^2 D^{-1}$. In physical units, $k_{on}^{0,*} = 1$ corresponds to $k_{on}^0 = 3.1 \times 10^6\,\rho_0^{-1}$ s^{-1}. Using the rates of eq 3, we calculate the probabilities p_{on}^i/p_{off}^i of forming/breaking a bond between nanoparticle i and the membrane, defined as

$$p_{on}^i = \frac{a_{on}^i}{a_{tot}},\ p_{off}^i = \frac{a_{off}^i}{a_{tot}} \tag{4}$$

$$a_{on}^i = n_i n^s k_{on}^i,\ a_{off}^i = n_i^s k_{off}^i \tag{5}$$

where a_{on}^i and a_{off}^i are the corresponding affinities, $a_{tot} = \sum_{i=1}^{N_p}(a_{on}^i + a_{off}^i)$, and N_p is the total number of nanoparticles in the simulation box. Using eq 4, we sample one of all possible reactions, along with the average time ($\bar{\tau}$) for it to happen (Prob($\bar{\tau}$) $\approx \exp[-\bar{\tau}/a_{tot}]$). We increment a reaction clock (τ_{reac}) by $\bar{\tau}$ ($\tau_{reac} = \tau_{reac} + \bar{\tau}$), and, if $\tau_{reac} < \Delta t$, then we update the values of $\{n_i, n_i^s, n^s\}$ and the affinities and probabilities (eqs 4 and 5), and then we fire another reaction until $\tau_{reac} > \Delta t$. Using the outcomes of the Gillespie algorithm at time Δt, we calculate forces using eq 2 and update nanoparticle positions using eq 1. At this point, we reiterate the algorithm starting from the calculation of the new on/off rates (eq 3).

To simulate the low dilution regimes used in experiments, we use grand canonical moves in which we insert/delete nanoparticles at the top layer of the simulation box. To simulate a fixed NP:LUV concentration ratio, we gradually decrease the chemical potential μ of the NPs as more of them are adsorbed by the membrane using $\mu = \mu_0 + \log(1 - n_{adh}/R_{NP:LUV})$, where μ_0, n_{adh}, and $R_{NP:LUV}$ are, respectively, a reference chemical potential, the number of adsorbed particles, and the stoichiometric ratio between NPs and LUVs. Grand canonical moves are necessary to make the simulations affordable but introduce a bias in the diffusion time required by nanoparticles to reach the membrane, making it significantly faster than in reality.

RESULTS AND DISCUSSION

We use DLS to investigate kinetic aspects of the interaction between NPs and LUVs decorated by DNA ligands and

DOI: 10.1021/acs.langmuir.8b02707
Langmuir XXXX, XXX, XXX−XXX

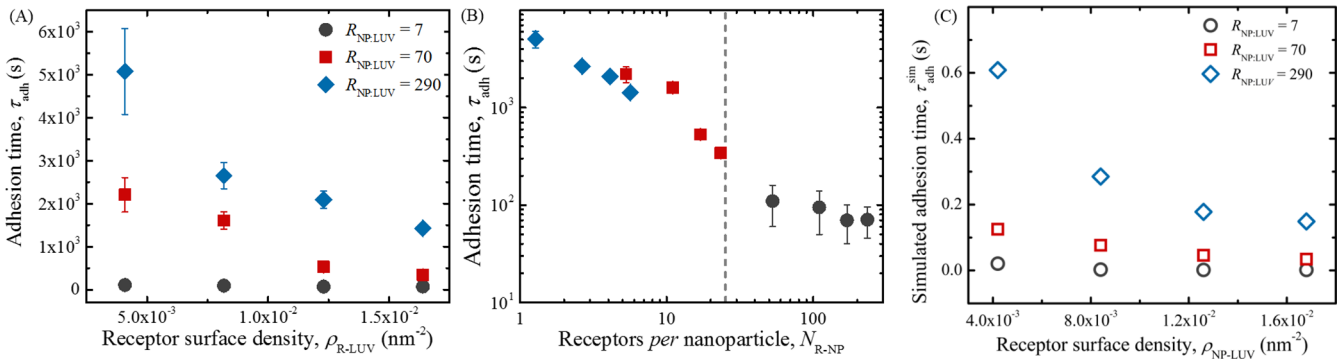

Figure 4. Adhesion kinetics depends on the receptor density and nanoparticle concentration. (A) Adhesion times τ_{adh} for three different NP:LUV concentration ratios $R_{NP:LUV}$ as a function of the receptor surface density ρ_{R-LUV}. (B) The same data as in panel A, shown as a function of the average number of receptors per NP in the system N_{R-NP}. The vertical dashed line marks the maximum number of bonds a nanoparticle can form as a result of geometrical limitations $N_{bonds}^{max} = 25$ (SI, section 7.1). (C) Simulated adhesion times τ_{adh}^{sim} using $\tau_{adh}^{sim} = -\Delta t/\log(1 - f(\Delta t))$, where $f(\Delta t)$ is the fraction of nanoparticles adsorbed at time Δt, with Δt being small enough to allow fitting the data with an exponential function. The predictions of panel A are larger than the values in panel B because the average time between consecutive NP−LUV encounters is smaller in simulations. Nevertheless, the similarity between the two datasets confirms that the reaction kinetics limits adsorption.

receptors (Figure 1) as a function of the receptor surface density on the LUVs, ρ_{R-LUV}, and the NP:LUV stoichiometric ratio, $R_{NP:LUV}$, spanning the ranges described in Table 1. In DLS experiments, the signal is dominated by the strongly scattering NPs, while owing to the similarity between the refractive index of the vesicles and that of the surrounding medium, the scattering contribution of the LUVs is comparatively negligible. (SI, section 5). When an individual NP adheres to a liposome whose size is approximately one order of magnitude larger, the dynamic diffusion coefficient of the nanoparticle is drastically reduced. After NPs are exposed to LUVs, this effect produces a progressive shift to longer decay times of the scattering autocorrelation function (ACF), as demonstrated in Figure 3A, which can thus be monitored to gain information on nanoparticle adhesion. For any measurement, we can identify two distinct NP populations: free nanoparticles and nanoparticles bound to the LUVs. Over time, the population of free NPs progressively shrinks while the bound population grows. Therefore, the measured ACF can be decomposed into the sum of two exponentials, one describing the free NP population and the second associated with membrane-bound NPs

$$\mathrm{ACF}(t, \tau) = A_{free}(t)e^{-(2\tau/\tau_{free})^{\alpha}} + A_{adh}(t)e^{-2\tau/\tau_{comp}} \quad (6)$$

where t is the time elapsed from the beginning of the experiment and τ indicates the delay time over which each scattering-intensity correlation is calculated. Time scales τ_{free} and τ_{comp} are related to the diffusion coefficient of the free NPs and the NP−LUV complexes, respectively, while $\alpha < 1$ follows from the polydispersity of the NP population.[77] Note that using a stretched exponential to model the contribution of the complexes did not improve the fits, and the stretching factor was always found to be comparable to 1. In eq 6, amplitudes $A_{free}(t)$ and $A_{adh}(t)$ are directly proportional to the number of free and adhering nanoparticles, which allows us to extract the fraction of bound nanoparticles as

$$f_{adh}(t) = \frac{A_{adh}(t)}{[A_{adh}(t) + A_{free}(t)]} \quad (7)$$

Equation 7 is valid under the assumption that free and membrane-bound NPs have the same scattering efficiency. This assumption is discussed in SI, section 6. Figure 3B demonstrates how f_{adh} increases with time as a stretched exponential

$$f_{adh}(t) = f_{adh}^{ss}\left[1 - \exp\left(-\frac{t}{\tau_{adh}}\right)^{\gamma}\right] \quad (8)$$

where τ_{adh} quantifies the typical adhesion time scales and the plateau value f_{adh}^{ss} represents the steady-state fraction of adsorbed nanoparticles. Optimal fitting is obtained by restricting the stretching factor γ in the ranges of 0.9−1, 0.6−0.7, and 0.4−0.5 for $R_{NP:LUV}$ = 7, 70, and 290, respectively. The stretched-exponential trend hints at hindered adsorption dynamics in which the rate of NP adhesion decreases over time. Similar trends have been ascribed to a number of processes including the depletion of adsorbing agents,[78,79] steric hindrance, and irreversible adsorption.[80] The progressive decrease in γ with increasing $R_{NP:LUV}$ that we observed indicates that the specific factor limiting adsorption in our system becomes more severe as the number of available nanoparticles increases. Note that in eq 6 parameters τ_{free} and α describe intrinsic characteristics of NPs that do not change over time and can therefore be independently determined and kept constant. The decay time τ_{comp} describes the diffusion of NP−LUV complexes, and evolution over the course of an experiment is analyzed in a dedicated section below.

Reaction-Limited Nanoparticle Adhesion and Receptor Depletion. Figure 4A demonstrates the dependence of the adhesion time τ_{adh} on the NP:LUV relative concentration ratio $R_{NP:LUV}$ and the surface density of DNA receptors on the LUVs ρ_{R-LUV}. For fixed ρ_{R-LUV}, τ_{adh} is observed to increase with increasing $R_{NP:LUV}$. If the latter is kept fixed, then τ_{adh} decreases monotonically with increasing ρ_{R-LUV}. The samples with the lowest $R_{NP:LUV}$, where τ_{adh} remains constant, constitute an exception. These trends can be better rationalized by studying the dependence of τ_{adh} on the number N_{R-NP} of receptors per NP, obtained by dividing the average number N_{R-LUV} of receptors anchored on each LUV by $R_{NP:LUV}$ (Table 1). The data in Figure 4B indeed show a smooth trend and clearly highlight two distinct regimes: τ_{adh} is low and constant for high N_{R-NP} while increasing monotonically as N_{R-NP} decreases below a threshold. The switching point coincides with $N_{R-NP} \approx 20-50$, which well matches the maximum number of ligand−receptor bonds that a single NP

DOI: 10.1021/acs.langmuir.8b02707
Langmuir XXXX, XXX, XXX−XXX

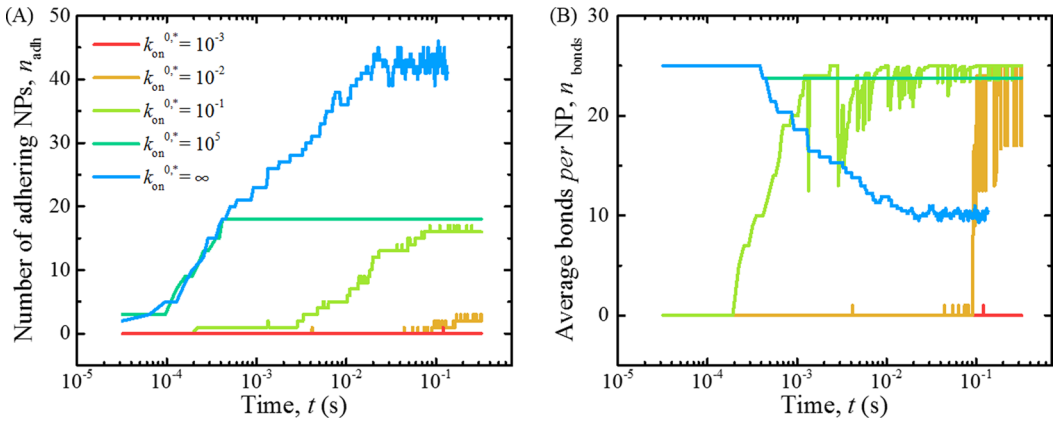

Figure 5. Simulations highlight the effect of kinetic rates on particle adhesion. (A) Number of adhering nanoparticles n_{adh} as a function of time for different reaction rates parametrized by $k_{on}^{0,*}$ (Simulation Algorithm section). When $k_{on}^{0,*} < \infty$, the system fails to reach the equilibrium state corresponding to the steady value of the $k_{on}^{0,*} = \infty$ trajectory. The receptors' surface density was set to $\rho_{R-LUV} = 4.2 \times 10^{-3}$ nm^{-2}, and the NP:LUV concentration ratio was $R_{NP:LUV} = 70$. (B) Average number of bonds n_{bonds} formed by each adhering nanoparticle for the simulated trajectories in panel A.

can form due to geometrical limitations, estimated as $N_{bonds}^{max} \approx 25$ (SI, section 7.1).

A qualitative explanation of the observed kinetic trends can be proposed by comparing the time scales of the individual processes leading to NP adhesion. Adsorption is initiated by a collision between a NP and a LUV, and the average time τ_{diff} between two of these events, at the beginning of the experiment, ranges from 80 to 450 ms (SI, section 8.1). However, during each collision, the NP−LUVs spend a much shorter time within their interaction range, $\tau_{coll} \approx l^2/D = 0.3$ μs. While a NP is in contact with a LUV, the time required for the formation of a ligand−receptor bond is $\tau_{bond} \lesssim 200$ ms (eq 3 and SI, section 8.2), indicating that several thousands of unsuccessful collisions n_{att} ($n_{att} \approx \tau_{bond}/\tau_{coll}$) are on average required for a NP to dock on a LUV. Assuming a collision rate on the order of $\sim\tau_{diff}^{-1}$ ($\tau_{diff} < 0.5$ s), the typical time scale at which particles start adsorbing can then be estimated using $n_{att}\tau_{diff} \approx 10^3-10^4$ s, which is compatible with Figure 4A. After the first bond is established, preventing the LUV and NP from diffusing apart, more connections are quickly formed as mobile receptors are converging toward the adhesion zone. Receptor accumulation occurs on the time scale of $\tau_{bond} \ll n_{att}\tau_{diff}$, so that before another NP has a chance to bind with the LUV, the first has already maximized the number of bonds, capturing N_{bonds}^{max} receptors. If N_{R-NP} exceeds N_{bonds}^{max}, then the process continues until all nanoparticles have formed N_{bonds}^{max} connections, leaving free receptors on the LUVs. In turn, for lower N_{R-NP}, the system enters a regime where the initially binding NPs quickly deplete receptors, drastically reducing their availability. Receptor scarcity causes τ_{bond} to increase, reducing the chances of a successful docking and substantially slowing down adhesion. In our experiments, receptor depletion is expected to be effectively irreversible because of the strong affinity between DNA ligands and receptors resulting in a bond breakup rate of $k_{off}^{i} \approx 10^6 \exp(\beta\Delta G_0)$ s^{-1} = 1.4×10^{-9} s^{-1} (eq 3). The initial transient, therefore, drives the system out of equilibrium. At a high NP:LUV concentration ratio of $R_{NP:LUV}$ = 290, steric hindrance can further limit nanoparticle adsorption at later stages given that at full packing a LUV can host a maximum of ∼150 NPs (SI, section 7.2).

These qualitative arguments can be verified by comparing experimental data with simulated trends. Figure 4C reports adhesion time scales τ_{adh}^{sim}, estimated by fitting the early stages of adsorption as detailed in the caption of Figure 4. Simulation results reproduce experimental trends in Figure 4A, supporting the interpretation that the reaction kinetics is the factor limiting NP adsorption in experiments. Note that in simulations the typical adhesion time scales are much faster than the experimental ones. This is due to the simulation scheme employed that, as compared to experiments, drastically reduces the time between successive NP−LUV encounters, τ_{diff}, while properly reproducing reaction times, τ_{bond}, and the time taken by NPs to diffuse away from the interacting region, τ_{coll}. This argument, along with the reasoning used above to justify the timescales of Figure 4A, explains the similarity between simulation and experimental profiles that differ only by a factor given by the ratio between the experimental and simulated τ_{diff}.

To better clarify the role played by the reaction rates in adsorption kinetics, in Figure 5A we visualize the time evolution of the number of adsorbed nanoparticles, calculated using different reaction rates. The latter are controlled by changing $k_{on}^{0,*}$ while keeping the ligand−receptor binding free energy, and therefore the thermodynamics of the system, constant. Consequently, the ligand−receptor off rate is also rescaled as $k_{off}^{i} \propto k_{on}^{0,*}$ (eq 3).

For $k_{on}^{0,*}$, $k_{off}^{i} = \infty$, the system experiences no kinetic hindrance from ligand−receptor reactions and can therefore reach thermodynamic equilibrium. Under these conditions, mobile receptors are observed to redistribute instantaneously among available NPs, progressively decreasing the average number of bonds per NP to stabilize a greater number of adsorbed nanoparticles, as displayed in Figure 5B. In turn, Figure 5A shows that for finite reaction rates the asymptotic number of adsorbed nanoparticles is much smaller than the one observed with $k_{on}^{0,*} = \infty$, implying that for $k_{on}^{0,*} < \infty$ the system fails to reach equilibrium. Indeed, even for the largest (finite) $k_{on}^{0,*}$ value we could test, k_{off}^{i} becomes negligibly small ($\sim 10^{-9}$ s^{-1}) owing to the strong ligand−receptor affinity. Bond irreversibility results in the receptor-depletion effect hypothesized above, where all adhering NPs quickly and irreversibly maximize the number of formed bonds, which in simulations is set to N_{bonds}^{max} = 25 (Figure 5B). To enter a regime where adsorption is not limited by DNA denaturation, one would

DOI: 10.1021/acs.langmuir.8b02707
Langmuir XXXX, XXX, XXX−XXX

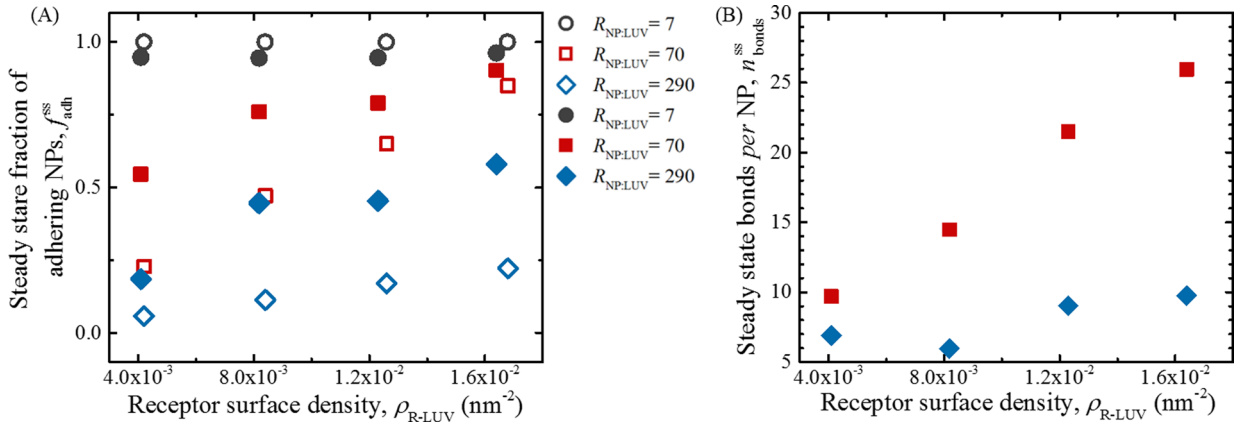

Figure 6. Receptor availability influences the steady-state configuration. (A) Steady-state fraction of adhering NPs f_{adh}^{ss} as estimated from experiments (full symbols) and simulations (empty symbols) as a function of $R_{NP:LUV}$ and ρ_{R-LUV}. (B) Experimental estimate of the steady-state average number of bonds per adhering NP n_{bonds}^{ss}.

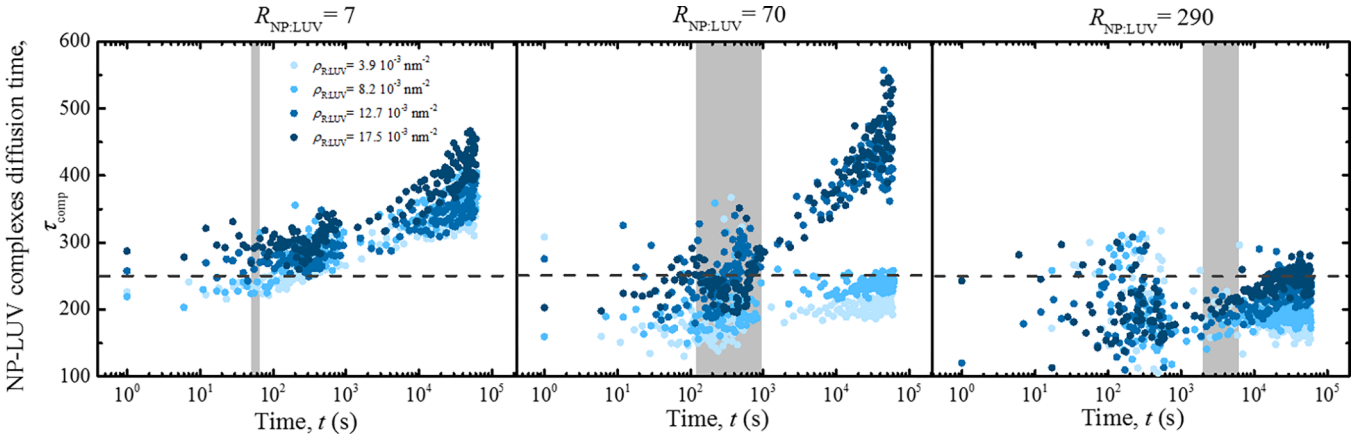

Figure 7. Diffusion time of NP−LUV complexes suggesting LUV clustering. Decay time τ_{comp} describing the diffusivity of NP−LUV complexes shown as a function of the receptor surface density on LUVs ρ_{R-LUV} for different NP:LUV concentration ratios $R_{NP:LUV}$ = 7, 70, and 290. The dashed lines represent the characteristic diffusion time of a 180-nm-diameter liposome. The gray areas mark the range of adhesion times τ_{adh} measured for the different ρ_{R-LUV} values (Figure 4).

need $k_{on}^{0,*} \gtrsim \exp[-\beta\Delta G_0]$. Unfortunately, such values of $k_{on}^{0,*}$ are not computationally affordable. For $k_{on}^{0,*} = \infty$, bond formation occurs instantly upon NP−LUV collision, implying that initial aggregation is diffusion-limited and occurs on a typical time scale of τ_{diff}. Figure 5 shows that, at early times, the curve calculated for $k_{on}^{0,*} = 10^5$ follows the same trend, indicating that, in this regime, the bond formation time τ_{bonds} is still significantly smaller than the collision time τ_{coll}. The same is no longer true if $k_{on}^{0,*} \leq 10^{-1}$, for which the onset of NP adhesion is significantly delayed as the likelihood of forming a permanent NP−LUV bond upon collision is progressively reduced.

Steady State. From the time evolution of the fraction $f_{adh}(t)$ of LUV-adhering NPs, we can extract the asymptotic value f_{adh}^{ss} corresponding to the fraction of adhering nanoparticles at steady state (eq 8). In Figure 6A, the experimental f_{adh}^{ss} is shown as a function of $R_{NP:LUV}$ and ρ_{R-LUV} (full symbols) and compared to simulation results (empty symbols). We observe qualitative agreement between experiments and simulations, but the latter appear to underestimate f_{adh}^{ss} in regimes of low N_{R-NP}. We ascribe this deviation to the fact that, in simulations, the average number of bonds N_{bonds}^{ss} formed by each adhering NP at steady state is always maximized and equal to N_{bonds}^{max} = 25 (Figure 5). This is not always the case in experiments, as shown in Figure 6B. N_{bonds}^{ss} is estimated experimentally by assuming that (i) all receptors are bound and (ii) receptors are evenly distributed among adsorbed NPs. We observe that the experimental N_{bonds}^{ss} is aways smaller than or comparable to N_{bonds}^{max}. More specifically, N_{bonds}^{ss} increases as a function of ρ_{R-LUV} for $R_{NP:LUV}$ = 70, approaching N_{bonds}^{max} for the highest tested receptor density while remaining relatively small and constant for $R_{NP:LUV}$ = 290. Note that condition (i) cannot be verified for $R_{NP:LUV}$ = 7, where $N_{R-NP} > N_{bonds}^{max}$, thus the estimates for these samples are not included in Figure 6. There are a number of effects that can result in $N_{bonds}^{ss} < N_{bonds}^{max}$, not accounted for in simulations. First, in Figure 6B we assume that receptors are evenly distributed among all of the adsorbed NPs, while it should not be excluded that those adhering at later stages may form fewer bonds than earlier nanoparticles. This nonideal behavior could emerge, for instance, as a consequence of nonselective (e.g., steric) interactions between ligands and receptors, which could significantly slow down bond formation and receptor sequestration by increasing τ_{bond}, allowing more nanoparticles to bind the LUV. Additionally, $N_{bonds}^{ss} < N_{bonds}^{max}$ may imply a degree of bond reversibility enabling receptor redistribution. This could be explained by an underestimation of the off rates, which in crowded environments may deviate sensibly from the

DOI: 10.1021/acs.langmuir.8b02707
Langmuir XXXX, XXX, XXX−XXX

theoretical predictions obtained under dilute conditions (eq 3).[81] We point out once again that for $R_{NP:LUV} = 290$ there is not enough room on the LUVs to accommodate all available nanoparticles, regardless of receptor availability. The geometrical limit to NP adsorption per LUV is ∼150, corresponding to $f_{adh} \approx 0.5$. This value is similar to the asymptotic fractions experimentally observed for $R_{NP:LUV} = 290$ in Figure 6A.

LUV Aggregation Driven by NP Bridging. Further information on the evolution of the system can be gathered by monitoring the time dependence of the diffusion time scale τ_{comp} of the NP−LUV complexes (eq 7). As shown in Figure 7, τ_{comp} exhibits different trends depending on ρ_{R-LUV} (shown in different colors) and $R_{NP:LUV}$ (shown in different panels). In all cases, τ_{comp} remains roughly constant for times shorter than the typical adhesion time scale τ_{adh}, marked as a gray-shaded band spanning the adhesion time scales observed for different ρ_{R-LUV} values. For $R_{NP:LUV} = 7$, an increase in τ_{adh} above the value expected for an individual LUV is observed at later times, suggesting the possibility of NP-mediated LUV−LUV aggregation. The latter can occur because, after all NPs are adsorbed, for $R_{NP:LUV} = 7$, the system still features free receptors that can bind NPs on other LUVs, causing aggregation. Consistently, the same phenomenon is observed for samples with $R_{NP:LUV} = 70$ and large receptor densities, which as demonstrated in Figure 6A also reach a regime where NPs are depleted but receptors are still available. As expected, in samples with $R_{NP:LUV} = 290$, LUVs remain monodisperse at all times because the large excess of NPs is always sufficient to deplete all receptors and effectively passivate the LUV surface against NP bridging. Note that LUV aggregation is not expected to affect our ability to quantify the fraction of bound NPs used to monitor adsorption kinetics: all NPs, whether adhering to an individual LUV or bridging two of them, would still be considered to be bound. In turn, NP-mediated LUV bridging may have an effect on the aggregation kinetics, as NPs can no longer be considered to be inactivated after adhering to a LUV and would still be able to sequestrate more receptors by forming LUV−NP−LUV bridges. However, in view of the faster diffusion kinetics of individual NPs compared to that of NP−LUV complexes, the adhesion of free NPs to LUVs is expected to dominate the formation of aggregates, as long as free NPs remain available.

CONCLUSIONS

Through a combination of dedicated experiments and coarse-grained simulations, we investigated the kinetics of adhesion of gold nanoparticles to artificial lipid vesicles mediated by nearly irreversible ligand−receptor bonds. DNA strands grafted onto the surface of the nanoparticles and the liposomes play the roles of both ligands and receptors. This model system is chosen to mimic interactions between nanoscale vectors and the surface of biological cells, a key process in several biological and medical scenarios, including cell invasion by viruses and parasites and cell targeting by means of synthetic nanomedical vectors. The rate of nanoparticle−vesicle adhesion is studied over a broad range of biologically and technologically relevant conditions by varying the surface density of available membrane-anchored receptors and the bulk concentration of nanoparticles. In both experiments and simulations, we find that adhesion rates are heavily suppressed in regimes where nanoparticles are present in excess compared to available receptors. Observed trends are rationalized by comparing the time scales of individual kinetic processes at play, including the frequency and duration of nanoparticle−vesicle collisions and the typical time required to form a ligand−receptor bond. We determine that the observed slow kinetics arises from receptor depletion as diffusive membrane-anchored receptors quickly segregate within the nanoparticle−vesicle adhesion region upon initial docking of individual nanoparticles. Nanoparticles adhering at early aggregation stages therefore sequestrate a significant proportion of the available receptors, reducing the rate of bond formation for late-coming nanoparticles and slowing down their adhesion. The near irreversibility of ligand−receptor connections hinders bond redistribution, leading to kinetically trapped configurations in which the number of membrane-adsorbed nanoparticles is not maximized.

Our observations have direct application in the design of medical nanovectors targeting cell membrane receptors: for a fixed receptor surface density, the adsorption rate of nanoscale probes can be maximized by improving the bond reversibility or by reducing the number of connections that each probe can form, delaying receptor depletion. Besides biomedical relevance, our remarks can also inform the design of multivalent colloidal building blocks for the bottom-up production of advanced materials, an area in which the predictability of the equilibrium phase behaviors is still not matched by similarly accurate control over relaxation kinetics. Our findings are also relevant to the modeling community. In particular, they highlight the importance of explicitly considering reaction rates when designing numerical simulations.

ASSOCIATED CONTENT

Supporting Information

The Supporting Information is available free of charge. The Supporting Information is available free of charge on the ACS Publications website at DOI: 10.1021/acs.langmuir.8b02707.

LUV characterization, gold nanoparticle characterization before and after DNA functionalization, quantification of the dissociation temperature in UV−vis experiments, simulation details, control experiments, optical model for calculating the scattering efficiency of a LUV covered by NPs, geometrical constrains, evaluation of timescales, and study of the interaction kinetics (PDF)

AUTHOR INFORMATION

Corresponding Authors

*E-mail: rl578@cam.ac.uk.
*E-mail: ld389@cam.ac.uk.
*E-mail: gbruylan@ulb.ac.be.

ORCID

Pietro Cicuta: 0000-0002-9193-8496
Bortolo Matteo Mognetti: 0000-0002-7960-8224
Lorenzo Di Michele: 0000-0002-1458-9747
Gilles Bruylants: 0000-0003-1752-5826

Notes

The authors declare no competing financial interest.

ACKNOWLEDGMENTS

R.L., B.M.M., P.C., L.D.M., and G.B. acknowledge support from the Wiener-Anspach Foundation. L.D.M. acknowledges support from the Leverhulme Trust and the Isaac Newton

DOI: 10.1021/acs.langmuir.8b02707
Langmuir XXXX, XXX, XXX−XXX

Trust through an Early Career Fellowship (ECF-2015-494) and the Royal Society through a University Research Fellowship (UF160152). P.C and L.D.M. acknowledge support from the EPSRC Programme Grant CAPITALS (EP/J017566/1). P.K.J. and B.M.M. are supported by the Fonds de la Recherche Scientifique de Belgique - FNRS under grant no. MIS F.4534.17. Computational resources have been provided by the Consortium des Équipements de Calcul Intensif (CECI), funded by the Fonds de la Recherche Scientifique de Belgique - FNRS under grant no. 2.5020.11. R.L. acknowledge Simon Croegaert for the production of AuNPs and TEM images, Jonathan Goole from the Pharmaceutics and Biopharmaceutics Group (Université Libre de Bruxelles) for providing access to the Malvern Zetasizer NanoZS, and Guy Vandenbussche from the Structure and Function of Biological Membranes Group (Université Libre de Bruxelles) for allowing the use of the ultracentrifuge. A dataset in support of this publication is available free of charge at https://doi.org/10.17863/CAM.35682.

REFERENCES

(1) Bidarimath, M.; Khalaj, K.; Kridli, R. T.; Kan, F. W. K.; Koti, M.; C, T. Extracellular vesicle mediated intercellular communication at the porcine maternal-fetal interface: A new paradigm for conceptus-endometrial cross-talk. *Sci. Rep.* **2017**, *7*, 40476.

(2) Tkach, M.; Théry, C. Communication by Extracellular Vesicles: Where We Are and Where We Need to Go. *Cell* **2016**, *164*, 1226−1232.

(3) Turturici, G.; Tinnirello, R.; Sconzo, G.; Geraci, F. Extracellular membrane vesicles as a mechanism of cell-to-cell communication: advantages and disadvantages. *American Journal of Physiology-Cell Physiology* **2014**, *306*, C621−C633.

(4) Nolte-'t Hoen, E.; Cremer, T.; Gallo, R. C.; Margolis, L. B. Extracellular vesicles and viruses: Are they close relatives? *Proc. Natl. Acad. Sci. U. S. A.* **2016**, *113*, 9155−9161.

(5) Rodrigues, M.; Fan, J.; Lyon, C.; Wan, M.; Hu, Y. Role of Extracellular Vesicles in Viral and Bacterial Infections: Pathogenesis, Diagnostics, and Therapeutics. *Theranostics* **2018**, *8*, 2709.

(6) Meckes, D. G.; Raab-Traub, N. Microvesicles and Viral Infection. *Journal of Virology* **2011**, *85*, 12844−12854.

(7) Zhang, S.; Gao, H.; Bao, G. Physical Principles of Nanoparticle Cellular Endocytosis. *ACS Nano* **2015**, *9*, 8655−8671.

(8) Straubinger, R. M.; Hong, K.; Friend, D. S.; Papahadjopoulos, D. Endocytosis of liposomes and intracellular fate of encapsulated molecules: Encounter with a low pH compartment after internalization in coated vesicles. *Cell* **1983**, *32*, 1069−1079.

(9) Ewers, H.; Helenius, A. Lipid-Mediated Endocytosis. *Cold Spring Harbor Perspect. Biol.* **2011**, *3*, a004721.

(10) Hillaireau, H.; Couvreur, P. Nanocarriers' entry into the cell: relevance to drug delivery. *Cell. Mol. Life Sci.* **2009**, *66*, 2873−2896.

(11) Vasir, J. K.; Labhasetwar, V. Quantification of the force of nanoparticle-cell membrane interactions and its influence on intracellular trafficking of nanoparticles. *Biomaterials* **2008**, *29*, 4244−4252.

(12) Lo, P. K.; Metera, K. L.; Sleiman, H. F. Self-assembly of three-dimensional DNA nanostructures and potential biological applications. *Curr. Opin. Chem. Biol.* **2010**, *14*, 597−607.

(13) Varilly, P.; Angioletti-Uberti, S.; Mognetti, B.; Frenkel, D. A general theory of DNA-mediated and other valence-limited colloidal interactions. *J. Chem. Phys.* **2012**, *137*, 094108−094122.

(14) Angioletti-Uberti, S.; Varilly, P.; Mognetti, B.; Tkachenko, A.; Frenkel, D. Communication: A simple analytical formula for the free energy of ligand-receptor-mediated interactions. *J. Chem. Phys.* **2013**, *138*, 021102−021106.

(15) Parolini, L.; Mognetti, B. M.; Kotar, J.; Eiser, E.; Cicuta, P.; Di Michele, L. Volume and porosity thermal regulation in lipid mesophases by coupling mobile ligands to soft membranes. *Nat. Commun.* **2015**, *6*, 5948.

(16) Shimobayashi, S. F.; Mognetti, B. M.; Parolini, L.; Orsi, D.; Cicuta, P.; Di Michele, L. Direct measurement of DNA-mediated adhesion between lipid bilayers. *Phys. Chem. Chem. Phys.* **2015**, *17*, 15615−15628.

(17) Di Michele, L.; Bachmann, S. J.; Parolini, L.; Mognetti, B. M. Communication: Free energy of ligand-receptor systems forming multimeric complexes. *J. Chem. Phys.* **2016**, *144*, 161104.

(18) Angioletti-Uberti, S.; Mognetti, B. M.; Frenkel, D. Theory and Simulation of DNA-Coated Colloids: a Guide for Rational Design. *Phys. Chem. Chem. Phys.* **2016**, *18*, 6373−6393.

(19) Bachmann, S. J.; Kotar, J.; Parolini, L.; Saric, A.; Cicuta, P.; Di Michele, L.; Mognetti, B. M. Melting transition in lipid vesicles functionalised by mobile DNA linkers. *Soft Matter* **2016**, *12*, 7804−7817.

(20) Bell, G.; Dembo, M.; Bongrand, P. Cell adhesion. Competition between nonspecific repulsion and specific bonding. *Biophys. J.* **1984**, *45*, 1051−1064.

(21) Coombs, D.; Dembo, M.; Wofsy, C.; Goldstein, B. Equilibrium Thermodynamics of Cell-Cell Adhesion Mediated by Multiple Ligand-Receptor Pairs. *Biophys. J.* **2004**, *86*, 1408−1423.

(22) Martinez-Veracoechea, F. J.; Frenkel, D. Designing super selectivity in multivalent nano-particle binding. *Proc. Natl. Acad. Sci. U. S. A.* **2011**, *108*, 10963−10968.

(23) Rogers, W. B.; Shih, W. M.; Manoharan, V. N. Using DNA to program the self-assembly of colloidal nanoparticles and microparticles. *Nature Reviews Materials* **2016**, *1*, 16008.

(24) Macfarlane, R. J.; O'Brien, M. N.; Petrosko, S. H.; Mirkin, C. A. Nucleic acid-modified nanostructures as programmable atom equivalents: forging a new "table of elements. *Angew. Chem., Int. Ed.* **2013**, *52*, 5688−5698.

(25) Jones, M. R.; Macfarlane, R. J.; Lee, B.; Zhang, J.; Young, K. L.; Senesi, A. J.; Mirkin, C. A. DNA-nanoparticle superlattices formed from anisotropic building blocks. *Nat. Mater.* **2010**, *9*, 913−917.

(26) Jones, M. R.; Seeman, N. C.; Mirkin, C. A. Programmable materials and the nature of the DNA bond. *Science* **2015**, *347*, 1260901.

(27) Nykypanchuk, D.; Maye, M. M.; van der Lelie, D.; Gang, O. DNA-guided crystallization of colloidal nanoparticles. *Nature* **2008**, *451*, 549−552.

(28) Chakraborty, I.; Meester, V.; van der Wel, C.; Kraft, D. J. Colloidal joints with designed motion range and tunable joint flexibility. *Nanoscale* **2017**, *9*, 7814−7821.

(29) Hong, S.; Leroueil, P. R.; Majoros, I. J.; Orr, B. G.; Baker, J. R.; Holl, M. M. B. The Binding Avidity of a Nanoparticle-Based Multivalent Targeted Drug Delivery Platform. *Chem. Biol.* **2007**, *14*, 107−115.

(30) Mammen, M. Polyvalent Interactions in Biological Systems: Implications for Design and Use of Multivalent Ligands and Inhibitors. *Angew. Chem., Int. Ed.* **1998**, *37*, 2754−2794.

(31) Cairo, C. W.; Gestwicki, J. E.; Kanai, M.; Kiessling, L. L. Control of Multivalent Interactions by Binding Epitope Density. *J. Am. Chem. Soc.* **2002**, *124*, 1615−1619.

(32) Carlson, C. B.; Mowery, P.; Owen, R. M.; Dykhuizen, E. C.; Kiessling, L. L. Selective Tumor Cell Targeting Using Low-Affinity, Multivalent Interactions. *ACS Chem. Biol.* **2007**, *2*, 119−127.

(33) Chaudhuri, A.; Battaglia, G.; Golestanian, R. The effect of interactions on the cellular uptake of nanoparticles. *Phys. Biol.* **2011**, *8*, 046002.

(34) Wibowo, A. S.; Singh, M.; Reeder, K. M.; Carter, J. J.; Kovach, A. R.; Meng, W.; Ratnam, M.; Zhang, F.; Dann, C. E. Structures of human folate receptors reveal biological trafficking states and diversity in folate and antifolate recognition. *Proc. Natl. Acad. Sci. U. S. A.* **2013**, *110*, 15180−15188.

(35) Leunissen, M. E.; Dreyfus, R.; Cheong, F. C.; Grier, D. G.; Sha, R.; Seeman, N. C.; Chaikin, P. M. Switchable self-protected attractions in DNA-functionalized colloids. *Nat. Mater.* **2009**, *8*, 590.

DOI: 10.1021/acs.langmuir.8b02707
Langmuir XXXX, XXX, XXX−XXX

(36) Leunissen, M. E.; Dreyfus, R.; Sha, R.; Seeman, N. C.; Chaikin, P. M. Quantitative Study of the Association Thermodynamics and Kinetics of DNA-Coated Particles for Different Functionalization Schemes. *J. Am. Chem. Soc.* **2010**, *132*, 1903−1913.
(37) Di Michele, L.; Varrato, F.; Kotar, J.; Nathan, S. H.; Foffi, G.; Eiser, E. Multistep kinetic self-assembly of DNA-coated colloids. *Nat. Commun.* **2013**, *4*, 1−7.
(38) Varrato, F.; Di Michele, L.; Belushkin, M.; Dorsaz, N.; Nathan, S. H.; Eiser, E.; Foffi, G. Arrested demixing opens route to bigels. *Proc. Natl. Acad. Sci. U. S. A.* **2012**, *109*, 19155−19160.
(39) Parolini, L.; Kotar, J.; Di Michele, L.; Mognetti, B. M. Controlling Self-Assembly Kinetics of DNA-Functionalized Liposomes Using Toehold Exchange Mechanism. *ACS Nano* **2016**, *10*, 2392−2398.
(40) Shenoy, V. B.; Freund, L. B. Growth and shape stability of a biological membrane adhesion complex in the diffusion-mediated regime. *Proc. Natl. Acad. Sci. U. S. A.* **2005**, *102*, 3213−3218.
(41) Atilgan, E.; Ovryn, B. Nucleation and growth of integrin adhesions. *Biophys. J.* **2009**, *96*, 3555−3572.
(42) Rogers, W. B.; Sinno, T.; Crocker, J. C. Kinetics and non-exponential binding of DNA-coated colloids. *Soft Matter* **2013**, *9*, 6412−6417.
(43) Licata, N. A.; Tkachenko, A. V. Kinetic limitations of cooperativity-based drug delivery systems. *Phys. Rev. Lett.* **2008**, *100*, 158102.
(44) Xu, Q.; Feng, L.; Sha, R.; Seeman, N.; Chaikin, P. Subdiffusion of a sticky particle on a surface. *Phys. Rev. Lett.* **2011**, *106*, 228102.
(45) Eze, N. A.; Sullivan, R. S.; Milam, V. T. Analysis of in Situ LNA and DNA Hybridization Events on Microspheres. *Biomacromolecules* **2017**, *18*, 1086−1096.
(46) Li, M.-H.; Choi, S. K.; Leroueil, P. R.; Baker, J. R. Evaluating Binding Avidities of Populations of Heterogeneous Multivalent Ligand-Functionalized Nanoparticles. *ACS Nano* **2014**, *8*, 5600−5609.
(47) Li, M.-H.; Zong, H.; Leroueil, P. R.; Choi, S. K.; Baker, J. R. Ligand Characteristics Important to Avidity Interactions of Multivalent Nanoparticles. *Bioconjugate Chem.* **2017**, *28*, 1649−1657.
(48) Beales, P. A.; Vanderlick, T. K. Specific binding of different vesicle populations by the hybridization of membrane-anchored DNA. *J. Phys. Chem. A* **2007**, *111*, 12372−12380.
(49) Hadorn, M.; Hotz, P. E. DNA-mediated self-assembly of artificial vesicles. *PLoS One* **2010**, *5*, e9886.
(50) Beales, P. A.; Nam, J.; Vanderlick, T. K. Specific adhesion between DNA-functionalized 'Janus' vesicles: size-limited clusters. *Soft Matter* **2011**, *7*, 1747−1755.
(51) Hadorn, M.; Boenzli, E.; Sørensen, K. T.; de Lucrezia, D.; Hanczyc, M. M.; Yomo, T. Defined DNA-mediated assemblies of gene-expressing giant unilamellar vesicles. *Langmuir* **2013**, *29*, 15309−15319.
(52) Pontani, L.-L.; Jorjadze, I.; Viasnoff, V.; Brujic, J. Biomimetic emulsions reveal the effect of mechanical forces on cell-cell adhesion. *Proc. Natl. Acad. Sci. U. S. A.* **2012**, *109*, 9839−9844.
(53) Feng, L.; Pontani, L.-L.; Dreyfus, R.; Chaikin, P.; Brujic, J. Specificity, flexibility and valence of DNA bonds guide emulsion architecture. *Soft Matter* **2013**, *9*, 9816−9823.
(54) Quinn, P.; Griffiths, G.; GRAHAM Warren, G. Density of newly synthesized plasma membrane proteins in intracellular membranes II. Biochemical studies. *J. Cell Biol.* **1984**, *98*, 2142−7.
(55) Lukeš, T.; Glatzová, D.; Kvíčalová, Z.; Levet, F.; Benda, A.; Letschert, S.; Sauer, M.; Brdička, T.; Lasser, T.; Cebecauer, M. Quantifying protein densities on cell membranes using super-resolution optical fluctuation imaging. *Nat. Commun.* **2017**, *8*, 1731.
(56) Banchelli, M.; Betti, F.; Berti, D.; Caminati, G.; Bombelli, F. B.; Brown, T.; Wilhelmsson, L. M.; Nordén, B.; Baglioni, P. Phospholipid Membranes Decorated by Cholesterol-Based Oligonucleotides as Soft Hybrid Nanostructures. *J. Phys. Chem. B* **2008**, *112*, 10942−10952.
(57) Bunge, A.; Loew, M.; Pescador, P.; Arbuzova, A.; Brodersen, N.; Kang, J.; Dähne, L.; Liebscher, J.; Herrmann, A.; Stengel, G.; Huster, D. Lipid Membranes Carrying Lipophilic Cholesterol-Based Oligonucleotides-Characterization and Application on Layer-by-Layer Coated Particles. *J. Phys. Chem. B* **2009**, *113*, 16425−16434.
(58) Czogalla, A.; Franquelim, H. G.; Schwille, P. DNA Nanostructures on Membranes as Tools for Synthetic Biology. *Biophys. J.* **2016**, *110*, 1698−1707.
(59) Kimling, J.; Maier, M.; Okenve, B.; Kotaidis, V.; Ballot, H.; Plech, A. Turkevich Method for Gold Nanoparticle Synthesis Revisited. *J. Phys. Chem. B* **2006**, *110*, 15700−15707.
(60) Mirkin, C.; Letsinger, R.; Mucic, R.; Storhoff, J. A DNA-based method for rationally assembling nanoparticles into macroscopic materials. *Nature* **1996**, *382*, 607−609.
(61) SantaLucia, J. A unified view of polymer, dumbbell, and oligonucleotide DNA nearest-neighbor thermodynamics. *Proc. Natl. Acad. Sci. U. S. A.* **1998**, *95*, 1460.
(62) Myers, B. D.; Lin, Q.-Y.; Wu, H.; Luijten, E.; Mirkin, C. A.; Dravid, V. P. Size-Selective Nanoparticle Assembly on Substrates by DNA Density Patterning. *ACS Nano* **2016**, *10*, 5679−5686.
(63) Kanayama, N.; Sekine, T.; Ozasa, K.; Kishi, S.; Nyu, T.; Hayashi, T.; Maeda, M. Terminal-Specific Interaction between Double-Stranded DNA Layers: Colloidal Dispersion Behavior and Surface Force. *Langmuir* **2016**, *32*, 13296−13304.
(64) Kim, Y.; Macfarlane, R. J.; Jones, M. R.; Mirkin, C. A. Transmutable nanoparticles with reconfigurable surface ligands. *Science* **2016**, *351*, 579−582.
(65) Doyen, M.; Bartik, K.; Bruylants, G. DNA-Promoted Auto-Assembly of Gold Nanoparticles: Effect of the DNA Sequence on the Stability of the Assemblies. *Polymers* **2013**, *5*, 1041−1055.
(66) Zhang, Y.; Zhou, H.; Ou-Yang, Z.-C. Stretching Single-Stranded DNA: Interplay of Electrostatic, Base-Pairing, and Base-Pair Stacking Interactions. *Biophys. J.* **2001**, *81*, 1133−1143.
(67) Bachmann, S. J.; Petitzon, M.; Mognetti, B. M. Bond formation kinetics affects self-assembly directed by ligand-receptor interactions. *Soft Matter* **2016**, *12*, 9585−9592.
(68) Zhdanov, V. P. Multivalent ligand-receptor-mediated interaction of small filled vesicles with a cellular membrane. *Phys. Rev. E: Stat. Phys., Plasmas, Fluids, Relat. Interdiscip. Top.* **2017**, *96*, 012408.
(69) Dasgupta, S.; Auth, T.; Gompper, G. Shape and orientation matter for the cellular uptake of nonspherical particles. *Nano Lett.* **2014**, *14*, 687−693.
(70) Tzlil, S.; Deserno, M.; Gelbart, W. M.; Ben-Shaul, A. A statistical-thermodynamic model of viral budding. *Biophys. J.* **2004**, *86*, 2037−2048.
(71) Schubertová, V.; Martinez-Veracoechea, F. J.; Vácha, R. Influence of ligand distribution on uptake efficiency. *Soft Matter* **2015**, *11*, 2726−2730.
(72) Di Michele, L.; Jana, P. K.; Mognetti, B. M. Steric interactions between mobile ligands facilitate complete wrapping in passive endocytosis. *Phys. Rev. E: Stat. Phys., Plasmas, Fluids, Relat. Interdiscip. Top.* **2018**, *98*, 032406.
(73) Angioletti-Uberti, S. Theory, simulations and the design of functionalized nanoparticles for biomedical applications: A Soft Matter Perspective. *npj Computational Materials* **2017**, *3*, 48.
(74) Šarić, A.; Cacciuto, A. Fluid Membranes Can Drive Linear Aggregation of Adsorbed Spherical Nanoparticles. *Phys. Rev. Lett.* **2012**, *108*, 118101.
(75) Parveen, N.; Rimkute, I.; Block, S.; Rydell, G. E.; Midtvedt, D.; Larson, G.; Hytönen, V. P.; Zhdanov, V. P.; Lundgren, A.; Höök, F. Membrane Deformation Induces Clustering of Norovirus Bound to Glycosphingolipids in a Supported Cell-Membrane Mimic. *J. Phys. Chem. Lett.* **2018**, *9*, 2278−2284.
(76) Gillespie, D. T. Exact stochastic simulation of coupled chemical reactions. *J. Phys. Chem.* **1977**, *81*, 2340−2361.
(77) Berne, B. J.; Pecora, R. *Dynamic Light Scattering with Applications to Chemistry, Biology, and Physics*; Dover Publications, 2000.
(78) Vasina, E. N.; Déjardin, P. Kinetics of Adsorption, Desorption, and Exchange of α-Chymotrypsin and Lysozyme on Poly(ethyleneterephthalate) Tracked Film and Track-Etched Membrane. *Biomacromolecules* **2003**, *4*, 304−313.

DOI: 10.1021/acs.langmuir.8b02707
Langmuir XXXX, XXX, XXX−XXX

(79) Douglas, J. F.; Johnson, H. E.; Granick, S. A Simple Kinetic Model of Polymer Adsorption and Desorption. *Science* **1993**, *262*, 2010−2012.
(80) Jia, L.; Lai, P. Kinetics and structure of irreversibly adsorbed polymer layers. *J. Chem. Phys.* **1996**, *105*, 11319−11325.
(81) Paramanathan, T.; Reeves, D.; Friedman, L. J.; Kondev, J.; Gelles, J. A general mechanism for competitor-induced dissociation of molecular complexes. *Nat. Commun.* **2014**, *5*, 5207.

DOI: 10.1021/acs.langmuir.8b02707
Langmuir XXXX, XXX, XXX−XXX